Linear density response function in the projector augmented wave method: Applications to solids, surfaces, and interfaces

Jun Yan, Jens. J. Mortensen, Karsten W. Jacobsen, and Kristian S. Thygesen*

Center for Atomic-scale Materials Design, Department of Physics, Technical University of Denmark, DK-2800 Kgs. Lyngby, Denmark

(Received 7 April 2011; revised manuscript received 11 May 2011; published 24 June 2011)

We present an implementation of the linear density response function within the projector-augmented wave method with applications to the linear optical and dielectric properties of both solids, surfaces, and interfaces. The response function is represented in plane waves while the single-particle eigenstates can be expanded on a real space grid or in atomic-orbital basis for increased efficiency. The exchange-correlation kernel is treated at the level of the adiabatic local density approximation (ALDA) and crystal local field effects are included. The calculated static and dynamical dielectric functions of Si, C, SiC, AlP, and GaAs compare well with previous calculations. While optical properties of semiconductors, in particular excitonic effects, are generally not well described by ALDA, we obtain excellent agreement with experiments for the surface loss function of graphene and the Mg(0001) surface with plasmon energies deviating by less than 0.2 eV. Finally, the method is applied to study the influence of substrates on the plasmon excitations in graphene.

DOI: 10.1103/PhysRevB.83.245122 PACS number(s): 73.20.Mf, 71.15.−m, 78.20.−e

I. INTRODUCTION

Time-dependent density functional theory (TDDFT)[1] has been widely used to calculate optical excitations in molecules and clusters as well as the optical and electron energy-loss spectra of bulk semiconductors, metals, and their surfaces.[2] The excitation energies and oscillator strengths of both single-particle and collective electronic excitations are determined by the frequency-dependent linear density response function $\chi(\mathbf{r},\mathbf{r}',\omega)$ giving the density response at point $\mathbf{r}$ to first order in a time-dependent perturbation of frequency ω applied at point $\mathbf{r}'$,

$$\delta n(\mathbf{r},\omega) = \int d\mathbf{r}\chi(\mathbf{r},\mathbf{r}',\omega)\delta V_{\text{ext}}(\mathbf{r}',\omega). \quad (1)$$

For finite systems, χ can be efficiently calculated by inverting an effective Hamiltonian in the space of particle-hole transitions. For the practically relevant case of frequency-independent exchange-correlation kernels this formulation leads to the well-known Casida equation.[3] For extended systems, it is more convinient to express χ in a basis of plane waves[4–6] where it has the generic form $\chi_{\mathbf{GG}'}(\mathbf{q},\omega)$, with $\mathbf{G}$ being reciprocal-lattice vectors and $\mathbf{q}$ being wave vectors in the first Brillouin zone (BZ).

In this paper we focus on the electronic response function of extended systems treating electron-electron interactions at the level of the random phase approximation (RPA) and the adiabatic local-density approximation (ALDA). For many extended systems such a description is insufficient to account for optical excitations because the electron-hole attraction is not properly accounted for. However, dielectric properties, in particular collective plasmon excitations, are generally accurately reproduced by this approach,[7,8] and quantitative agreement with electron energy-loss experiments have been reported for bulk metals,[9,10] surfaces,[11,12] graphene-based systems,[13,14] semiconductors,[15,16] and even supercondutors.[17] Furthermore, the accurate evaluation of the density response function at the RPA or ALDA level is a prerequisite for implementation of most post-DFT schemes, such as RPA correlation energy,[18] exact-exchange optimized-effective-potential methods,[19] the GW approximation for quasiparticle excitations,[20,21] and the Bethe-Salpeter equation[21,22] for optical excitations.

Here we present an implementation of the density response function within the electronic structure code GPAW,[23,24] which is based on the projector augmented wave (PAW) methodology[25,26] and represents wave functions on real-space grids or in terms of linear combinations of atomic orbitals (LCAO).[27] Within the PAW formalism one works implicitly with the all-electron wave functions and has access to the (frozen) core states. This makes the method applicable to a very broad range of systems including materials with strongly localized d or f electrons, which can be problematic to describe with pseudopotentials. An additional advantage of the PAW formalism, with respect to linear-response theory, is that the optical transition operator in the long-wavelength limit can be obtained directly due to the use of all-electron wave functions.[28] The noninteracting response function χ^0 is built from the single-particle eigenstates obtained either on a real-space grid, which is the standard representation in the GPAW code, or in terms of a localized atomic-orbital (LCAO) basis. We have found that the latter choice reduces the computational cost of χ^0 considerably while still preserving the high accuracy of the grid calculation.

The method is used to calculate the macroscopic dielectric constants of a number of bulk semiconductors, showing very good agreement with previous calculations as well as experiments. For the surface plasmons of the Mg(0001) surface we find, in agreement with previous studies, that the ALDA kernel lowers the plasmon energies by around 0.3 eV relative to the RPA values and thereby reduces the deviation from experiments from 4% to 1–2%. Very good agreement with experiments is also found for the plasmon energies of graphene, which are shown to exhibit a linear dispersion with a value of 4.9 eV in the long-wavelength limit. The deposition of graphene on a SiC substrate is shown to have little effect on the plasmon energies but leads to significant broadening of the plasmon resonances. In contrast, deposition on an Al surface completely quenches the graphene plasmons due to strong nonlocal electronic screening.

The rest of this paper is organized as follows. Section II introduces the theoretical framework, where the PAW methodology, the density response function for both finite $\mathbf{q}$ and $\mathbf{q} \to 0$, and the ALDA kernel in the PAW method are discussed. The details of the implementation and parallelization in GPAW and other technical details are presented in Sec. III. Section IV presents applications for optical properties and plasmon excitations of bulk and surfaces, where comparison with other calculations and experiments are given. Our recent investigation on the effect of a semiconducting and metallic substrate on the plasmon excitations in graphene is also briefly discussed in this section. Finally, a summary is given in Sec. V.

II. METHOD

A. Basics of the PAW formalism

In the PAW formalism,[25,26] a true all-electron Kohn-Sham wave function $\psi_{n\mathbf{k}}$ is obtained by a linear transformation from a smooth pesudo-wave function $\tilde{\psi}_{n\mathbf{k}}$ via $\psi_{n\mathbf{k}} = \hat{T}\tilde{\psi}_{n\mathbf{k}}$. The transformation operator is chosen in such a way that the all-electron wave function $\psi_{n\mathbf{k}}$ is the sum of the pseudo one $\tilde{\psi}_{n\mathbf{k}}$ and an additive contribution centered around each atom written as

$$\psi_{n\mathbf{k}}(\mathbf{r}) = \tilde{\psi}_{n\mathbf{k}}(\mathbf{r}) + \sum_{a,i} \langle \tilde{p}_i^a | \tilde{\psi}_{n\mathbf{k}} \rangle \left[\phi_i^a(\mathbf{r} - \mathbf{R}_a) - \tilde{\phi}_i^a(\mathbf{r} - \mathbf{R}_a) \right]. \tag{2}$$

The pseudo-wave function $\tilde{\psi}_{n\mathbf{k}}$ matches the all-electron one $\psi_{n\mathbf{k}}$ outside the augmentation spheres centered on each atom a at position $\mathbf{R}_a$. Their differences inside the augmentation region are expanded on atom-centered all-electron partial waves ϕ_i^a and the smooth counterparts $\tilde{\phi}_i^a$. The expansion coefficient is given by $\langle \tilde{p}_i^a | \tilde{\psi}_{n\mathbf{k}} \rangle$, where $\tilde{p}_i^a$ is chosen as a dual basis to the pseudopartial wave and is called a projector function. A frequently occurring term is the all-electron expectation value for a semilocal operator A written as

$$\langle \psi_{n\mathbf{k}} | A | \psi_{n\mathbf{k}} \rangle = \langle \tilde{\psi}_{n\mathbf{k}} | A | \tilde{\psi}_{n\mathbf{k}} \rangle + \sum_{a,ij} \langle \tilde{\psi}_{n\mathbf{k}} | \tilde{p}_i^a \rangle \langle \tilde{p}_j^a | \tilde{\psi}_{n\mathbf{k}} \rangle \times \left[\langle \phi_i^a | A | \phi_j^a \rangle - \langle \tilde{\phi}_i^a | A | \tilde{\phi}_j^a \rangle \right]. \tag{3}$$

B. Density response function and dielectric matrix

A key concept in TDDFT is the density response function χ. It is defined as $\chi(\mathbf{r},\mathbf{r}',\omega) = \delta n(\mathbf{r},\omega)/\delta V_{\text{ext}}(\mathbf{r}',\omega)$, where V_{ext} is the external perturbing potential and δn is the induced density under the perturbation. For periodic systems, χ can be written in the form

$$\chi(\mathbf{r},\mathbf{r}',\omega) = \frac{1}{N_q \Omega} \sum_{\mathbf{q}}^{\text{BZ}} \sum_{\mathbf{G}\mathbf{G}'} e^{i(\mathbf{q}+\mathbf{G})\cdot\mathbf{r}} \chi_{\mathbf{G}\mathbf{G}'}(\mathbf{q},\omega) e^{-i(\mathbf{q}+\mathbf{G}')\cdot\mathbf{r}'}, \tag{4}$$

where $\mathbf{G},\mathbf{G}'$ are reciprocal-lattice vectors, $\mathbf{q}$ is a wave vector restricted to the first Brillouin zone (BZ), N_q is the number of $\mathbf{q}$ vectors, and Ω is the volume of the real-space primitive cell.

The density response function of the interacting electron system, χ, can be obtained from the noninteracting density response function of the Kohn-Sham system, χ^0, and a kernel K describing the electron-electron interactions by solving a Dyson-like equation

$$\chi_{\mathbf{G}\mathbf{G}'}(\mathbf{q},\omega) = \chi^0_{\mathbf{G}\mathbf{G}'}(\mathbf{q},\omega) + \sum_{\mathbf{G}_1\mathbf{G}_2} \chi^0_{\mathbf{G}\mathbf{G}_1}(\mathbf{q},\omega) K_{\mathbf{G}_1\mathbf{G}_2}(\mathbf{q}) \chi_{\mathbf{G}_2\mathbf{G}'}(\mathbf{q},\omega). \tag{5}$$

The expression for the noninteracting density response function in the Bloch representation of Adler and Wiser[4,5] is

$$\chi^0_{\mathbf{G}\mathbf{G}'}(\mathbf{q},\omega) = \frac{2}{\Omega} \sum_{\mathbf{k},nn'} (f_{n\mathbf{k}} - f_{n'\mathbf{k}+\mathbf{q}}) \frac{n_{n\mathbf{k},n'\mathbf{k}+\mathbf{q}}(\mathbf{G}) n^*_{n\mathbf{k},n'\mathbf{k}+\mathbf{q}}(\mathbf{G}')}{\omega + \epsilon_{n\mathbf{k}} - \epsilon_{n'\mathbf{k}+\mathbf{q}} + i\eta}, \tag{6}$$

where

$$n_{n\mathbf{k},n'\mathbf{k}+\mathbf{q}}(\mathbf{G}) \equiv \langle \psi_{n\mathbf{k}} | e^{-i(\mathbf{q}+\mathbf{G})\cdot\mathbf{r}} | \psi_{n'\mathbf{k}+\mathbf{q}} \rangle \tag{7}$$

is defined as the charge-density matrix. Its evaluation within the PAW formalism is explained in detail in the following subsection. $\epsilon_{n\mathbf{k}}$, $f_{n\mathbf{k}}$, and $\psi_{n\mathbf{k}}$ are the Kohn-Sham eigen-energy, occupation, and wave function for band index n and wave vector $\mathbf{k}$, and η is a broadening parameter. The summation over $\mathbf{k}$ runs all over the BZ and $\sum_{\mathbf{k}} f_{n\mathbf{k}} = 1$ is satisfied for the occupied states. The factor of 2 accounts for spin (we assume a spin-degenerate system).

The kernel in Eq. (5) consists of both a Coulomb and an exchange-correlation (xc) part. The Coulomb kernel is diagonal in the Bloch representation and written as

$$K^{\text{C}}_{\mathbf{G}_1\mathbf{G}_2}(\mathbf{q}) = \frac{4\pi}{|\mathbf{q}+\mathbf{G}_1|^2} \delta_{\mathbf{G}_1\mathbf{G}_2}, \tag{8}$$

while the xc kernel evaluated within ALDA is given by

$$K^{\text{xc-ALDA}}_{\mathbf{G}_1\mathbf{G}_2}(\mathbf{q}) = \frac{1}{\Omega} \int d\mathbf{r}\, f_{\text{xc}}[n(\mathbf{r})] e^{-i(\mathbf{G}_1-\mathbf{G}_2)\cdot\mathbf{r}}, \tag{9}$$

with

$$f_{\text{xc}}[n(\mathbf{r})] = \left. \frac{\partial^2 E_{\text{xc}}[n]}{\partial n^2} \right|_{n_0(\mathbf{r})}. \tag{10}$$

Details on the evaluation of the xc kernel in the PAW method can be found in a following subsection.

The Fourier transform of the microscopic dielectric matrix, defined as $\epsilon^{-1}(\mathbf{r},\mathbf{r}',\omega) = \delta V_{\text{tot}}(\mathbf{r},\omega)/\delta V_{\text{ext}}(\mathbf{r}',\omega)$, is related to the density response function via

$$\epsilon^{-1}_{\mathbf{G}\mathbf{G}'}(\mathbf{q},\omega) = \delta_{\mathbf{G}\mathbf{G}'} + \frac{4\pi}{|\mathbf{q}+\mathbf{G}|^2} \chi_{\mathbf{G}\mathbf{G}'}(\mathbf{q},\omega), \tag{11}$$

where χ is obtained from χ^0 according to Eq. (5). The off-diagonal elements of the $\chi^0_{\mathbf{G}\mathbf{G}'}$ matrix describes the response of the electrons at wave vectors different from the external perturbing field and thus contain information about the inhomogeneity of the microscopic response of electrons known as the "local field effect."[6] The macroscopic dielectric function is defined as

$$\epsilon_M(\mathbf{q},\omega) = \frac{1}{\epsilon^{-1}_{\mathbf{0}\mathbf{0}}(\mathbf{q},\omega)}, \tag{12}$$

and is directly related to many experimental properties. For example, the optical-absorption spectrum (ABS) is given by

$\mathrm{Im}\epsilon_M(\mathbf{q}\to 0,\omega)$. The electron energy-loss spectrum (EELS[29]) is proportional to $-\mathrm{Im}(1/\epsilon_M)$. Both spectra reveal information about the elementary electronic excitations of the system. EELS is especially useful in probing the collective electronic excitations, known as plasmons, of bulk and low-dimensional systems.[29]

C. Charge-density matrix in the PAW method

In this subsection, we will discuss the charge-density matrix $n_{n\mathbf{k},n'\mathbf{k}+\mathbf{q}}(\mathbf{G})$, which is defined in Eq. (7) and is a crucial quantity for the evaluation of χ^0. Care must be taken for the long-wavelength limit ($\mathbf{q}\to 0$) since the Coulomb kernel, $4\pi/|\mathbf{q}+\mathbf{G}|^2$, diverges at $\mathbf{q}\to 0$ and $\mathbf{G}=0$; while the charge-density matrix approaches zero at this limit. As a result, we separate the discussion into two parts: finite $\mathbf{q}$ and $\mathbf{q}\to 0$.

1. Finite q

Considering the transformation between the pseudo-wave function and the all-electron wave function in Eq. (2) and employing Eq. (3) yields

$$n_{n\mathbf{k},n'\mathbf{k}+\mathbf{q}}(\mathbf{G}) = \tilde{n}_{n\mathbf{k},n'\mathbf{k}+\mathbf{q}}(\mathbf{G}) + \sum_{a,ij}\langle\tilde{\psi}_{n\mathbf{k}}|\tilde{p}_i^a\rangle\langle\tilde{p}_j^a|\tilde{\psi}_{n'\mathbf{k}+\mathbf{q}}\rangle Q_{ij}^a(\mathbf{q}+\mathbf{G}) \quad (13)$$

with

$$\tilde{n}_{n\mathbf{k},n'\mathbf{k}+\mathbf{q}}(\mathbf{G}) \equiv \langle\tilde{\psi}_{n\mathbf{k}}|e^{-i(\mathbf{q}+\mathbf{G})\cdot\mathbf{r}}|\tilde{\psi}_{n'\mathbf{k}+\mathbf{q}}\rangle \quad (14)$$

$$Q_{ij}^a(\mathbf{K}) \equiv \langle\phi_i^a|e^{-i\mathbf{K}\cdot\mathbf{r}}|\phi_j^a\rangle - \langle\tilde{\phi}_i^a|e^{-i\mathbf{K}\cdot\mathbf{r}}|\tilde{\phi}_j^a\rangle \quad (15)$$

and $\mathbf{K}\equiv\mathbf{q}+\mathbf{G}$.

The pseudodensity matrix in Eq. (14) is calculated using a mixed space scheme. First, the cell periodic function $\tilde{\psi}^*_{n\mathbf{k}}(\mathbf{r})\tilde{\psi}_{n'\mathbf{k}+\mathbf{q}}(\mathbf{r})e^{-i\mathbf{q}\cdot\mathbf{r}}$ is evaluated on a real-space grid; then it is Fourier transformed to get

$$\tilde{n}_{n\mathbf{k},n'\mathbf{k}+\mathbf{q}}(\mathbf{G}) = \mathcal{F}[\tilde{\psi}^*_{n\mathbf{k}}(\mathbf{r})\tilde{\psi}_{n'\mathbf{k}+\mathbf{q}}(\mathbf{r})e^{-i\mathbf{q}\cdot\mathbf{r}}]. \quad (16)$$

The augmentation part in Eq. (15) is calculated on fine one-dimensional radial grids centered on each atom. Such fine grids are required to represent accurately the oscillating nature of the all-electron partial wave in the augmentation region. The plane-wave term $e^{-i\mathbf{K}\cdot\mathbf{r}}$ is expanded using real spherical harmonics by

$$e^{-i\mathbf{K}\cdot\mathbf{r}} = 4\pi\sum_{lm}(-i)^l j_l(|\mathbf{K}|r)Y_{lm}(\hat{\mathbf{r}})Y_{lm}(\hat{\mathbf{K}}), \quad (17)$$

where j_l is the spherical Bessel function for angular momentum l and $\hat{\mathbf{K}}=\mathbf{K}/|\mathbf{K}|$. Combining the above equations and the expression for the partial wave $|\phi_i^a\rangle = \phi^a_{n_il_i}(r)Y_{l_im_i}(\hat{\mathbf{r}})$, we can write

$$Q_{ij}^a(\mathbf{K}) = 4\pi e^{-i\mathbf{K}\cdot\mathbf{R}_a}\sum_{lm}(-i)^l Y_{lm}(\hat{\mathbf{K}})\int d\hat{\mathbf{r}}\; Y_{lm}Y_{l_im_i}Y_{l_jm_j} \times\int dr\; r^2 j_l(|\mathbf{K}|r)\left[\phi^a_{n_il_i}(r)\phi^a_{n_jl_j}(r) - \tilde{\phi}^a_{n_il_i}(r)\tilde{\phi}^a_{n_jl_j}(r)\right]. \quad (18)$$

2. Long-wavelength limit

In the long-wavelength limit, the $\mathbf{G}\neq 0$ components of the density matrix $n_{n\mathbf{k},n'\mathbf{k}+\mathbf{q}}(\mathbf{G})$ remain the same as that for finite $\mathbf{q}$. Only the $\mathbf{G}=0$ components need to be modified and are written as

$$n_{n\mathbf{k},n'\mathbf{k}+\mathbf{q}}(0)|_{\mathbf{q}\to 0} \equiv \langle\psi_{n\mathbf{k}}|e^{-i\mathbf{q}\cdot\mathbf{r}}|\psi_{n'\mathbf{k}+\mathbf{q}}\rangle_{\mathbf{q}\to 0}. \quad (19)$$

In Ref. 30, the above so-called longitudinal form is derived in the PAW framework by using Taylor expansion of the $e^{i\mathbf{q}\cdot\mathbf{r}}$ to the first order. Here we adopt an alternative but equivalent form, which can be derived using the second-order $k\cdot p$ perturbation theory[31] as described below.

Expressing the wave function using Bloch's theorem as $\psi_{n\mathbf{k}}(\mathbf{r}) = u_{n\mathbf{k}}(\mathbf{r})e^{i\mathbf{k}\cdot\mathbf{r}}$, where $u_{n\mathbf{k}}(\mathbf{r})$ is the periodic Bloch wave, the dipole transition element in Eq. (19) becomes

$$\langle\psi_{n\mathbf{k}}|e^{-i\mathbf{q}\cdot\mathbf{r}}|\psi_{n'\mathbf{k}+\mathbf{q}}\rangle = \langle u_{n\mathbf{k}}|u_{n'\mathbf{k}+\mathbf{q}}\rangle. \quad (20)$$

For vanishing $\mathbf{q}$, the wave function for $|u_{n'\mathbf{k}+\mathbf{q}}\rangle$ can be obtained in terms of those for $|u_{m\mathbf{k}}\rangle$ through second-order perturbation theory:

$$|u_{n'\mathbf{k}+\mathbf{q}}\rangle = |u_{n'\mathbf{k}}\rangle + \sum_{m\neq n'}\frac{\langle\psi_{m\mathbf{k}}|\tilde{V}|u_{n'\mathbf{k}}\rangle}{\epsilon_{n'\mathbf{k}}-\epsilon_{m\mathbf{k}}}|u_{m\mathbf{k}}\rangle. \quad (21)$$

The perturbing potential $\tilde{V}$ in the above equation is obtained through

$$\tilde{V} = H(\mathbf{k}+\mathbf{q}) - H(\mathbf{k}) = -i\mathbf{q}\cdot(\nabla + i\mathbf{k}), \quad (22)$$

where

$$H(\mathbf{k}) = -\tfrac{1}{2}(\nabla + i\mathbf{k})^2 + V(\mathbf{r}) \quad (23)$$

is the $k\cdot p$ Hamiltonian[31] and $V(\mathbf{r})$ is the effective Kohn-Sham potential.

Combining Eqs. (20)–(22), the charge-density matrix at the long-wavelength limit becomes

$$n_{n\mathbf{k},n'\mathbf{k}+\mathbf{q}}(0)|_{\mathbf{q}\to 0} = \frac{-i\mathbf{q}\cdot\langle n_{n\mathbf{k}}|\nabla + i\mathbf{k}|u_{n'\mathbf{k}}\rangle}{\epsilon_{n'\mathbf{k}}-\epsilon_{n\mathbf{k}}}, = \frac{-i\mathbf{q}\cdot\langle\psi_{n\mathbf{k}}|\nabla|\psi_{n'\mathbf{k}}\rangle}{\epsilon_{n'\mathbf{k}}-\epsilon_{n\mathbf{k}}}. \quad (24)$$

The above expression for the charge-density matrix in the PAW method has an advantage over the pseudopotential method, where the nabla operator has to be corrected by the commutator of the nonlocal part of pseudopotential with the position operator $\mathbf{r}$.[28] In the PAW method, the matrix element $\langle\psi_{n\mathbf{k}}|\nabla|\psi_{n'\mathbf{k}}\rangle$ is given by

$$\langle\psi_{n\mathbf{k}}|\nabla|\psi_{n'\mathbf{k}}\rangle = \langle\tilde{\psi}_{n\mathbf{k}}|\nabla|\tilde{\psi}_{n'\mathbf{k}}\rangle + \sum_{a,ij}\langle\tilde{\psi}_{n\mathbf{k}}|\tilde{p}_i^a\rangle\langle\tilde{p}_j^a|\tilde{\psi}_{n'\mathbf{k}}\rangle \times\left[\langle\phi_i^a|\nabla|\phi_j^a\rangle - \langle\tilde{\phi}_i^a|\nabla|\tilde{\phi}_j^a\rangle\right]. \quad (25)$$

In GPAW, where the pseudo-wave functions $\tilde{\psi}_{n\mathbf{k}}$ are represented on a real-space grid, the first matrix element is calculated using a finite difference approximation for the nabla operator. The augmentation part is evaluated on

fine one-dimensional radial grids. The nabla operator combined with partial waves $\phi_i^a(\mathbf{r}) = \phi_{n_1 l_1}^a(r) Y_{l_1 m_1}(\hat{\mathbf{r}})$ and $\phi_j^a(\mathbf{r}) = \phi_{n_2 l_2}^a(r) Y_{l_2 m_2}(\hat{\mathbf{r}})$ is written as

$$\langle \phi_i^a | \nabla | \phi_j^a \rangle = \left\langle \phi_i^a \middle| \frac{\partial}{\partial r} \left(\frac{\phi_{n_2 l_2}^a}{r^{l_2}} \right) \frac{\partial r}{\partial \mathbf{r}} r^{l_2} Y_{l_2 m_2} \right\rangle + \left\langle \phi_i^a \middle| \frac{\phi_{n_2 l_2}^a}{r^{l_2}} \nabla \left(r^{l_2} Y_{l_2 m_2} \right) \right\rangle. \quad (26)$$

Since real spherical harmonics are employed, we get

$$\frac{\partial r}{\partial \mathbf{r}} = \left(\frac{x}{r}, \frac{y}{r}, \frac{z}{r} \right) = \sqrt{\frac{4\pi}{3}} \left(Y_{1m_x}, Y_{1m_y}, Y_{1m_z} \right). \quad (27)$$

Substitute the above equation into Eq. (26) and split the integration into radial and angular parts, we get for the x component

$$\langle \phi_i^a | \frac{\partial}{\partial x} | \phi_j^a \rangle = \sqrt{\frac{4\pi}{3}} \int dr\, r^2 \phi_{n_1 l_1}^a \frac{\partial}{\partial r} \left(\frac{\phi_{n_2 l_2}^a}{r^{l_2}} \right) r^{l_2} \int d\hat{\mathbf{r}}\, Y_{l_1 m_1} Y_{l_2 m_2} Y_{1 m_x} + \int dr\, r^2 \phi_{n_1 l_1}^a \frac{\phi_{n_2 l_2}^a}{r} \int d\hat{\mathbf{r}}\, Y_{l_1 m_1} r^{1-l_2} \frac{\partial}{\partial x} \left(r^{l_2} Y_{l_2 m_2} \right). \quad (28)$$

The derivation for the y and z component and for the pseudo-partial wave follows in a similar way.

D. ALDA xc kernel in the PAW method

The ALDA xc kernel, expressed in Eq. (9), is evaluated using the all-electron density, which takes the form

$$n(\mathbf{r}) = \tilde{n}(\mathbf{r}) + \sum_a [n^a(\mathbf{r} - \mathbf{R}_a) - \tilde{n}^a(\mathbf{r} - \mathbf{R}_a)], \quad (29)$$

where

$$\tilde{n}(\mathbf{r}) = \sum_{n\mathbf{k}} f_{n\mathbf{k}} |\tilde{\psi}_{n\mathbf{k}}(\mathbf{r})|^2 + \sum_a \tilde{n}_c^a(|\mathbf{r} - \mathbf{R}_a|), \quad (30)$$

$$n^a(\mathbf{r}) = \sum_{ij} D_{ij}^a \phi_i^a(\mathbf{r}) \phi_j^a(\mathbf{r}) + n_c^a(\mathbf{r}), \quad (31)$$

$$\tilde{n}^a(\mathbf{r}) = \sum_{ij} D_{ij}^a \tilde{\phi}_i^a(\mathbf{r}) \tilde{\phi}_j^a(\mathbf{r}) + \tilde{n}_c^a(\mathbf{r}), \quad (32)$$

with $D_{ij}^a = \sum_{n\mathbf{k}} \langle \tilde{\psi}_{n\mathbf{k}} | \tilde{p}_i^a \rangle f_{n\mathbf{k}} \langle \tilde{p}_j^a | \tilde{\psi}_{n\mathbf{k}} \rangle$. Here $n_c^a(\mathbf{r})$ is the all-electron core density and $\tilde{n}_c^a(\mathbf{r})$ can be chosen as any smooth continuation of $n_c^a(\mathbf{r})$ inside the augmentation sphere since it will be canceled out in Eq. (30).

The ALDA xc kernel can also be separated into smooth and atom-centered contributions,

$$K_{\mathbf{G}_1\mathbf{G}_2}^{\mathrm{xc-ALDA}} = \tilde{K}_{\mathbf{G}_1\mathbf{G}_2}^{\mathrm{xc-ALDA}} + \sum_a \Delta K_{\mathbf{G}_1\mathbf{G}_2}^{a,\mathrm{xc-ALDA}}. \quad (33)$$

The smooth part is constructed from pseudodensity and by utilizing a Fourier transform

$$\tilde{K}_{\mathbf{G}_1\mathbf{G}_2}^{\mathrm{xc-ALDA}} = \frac{1}{\Omega} \int d\mathbf{r}\, f_{\mathrm{xc}}[\tilde{n}(\mathbf{r})] e^{-i(\mathbf{G}_1 - \mathbf{G}_2)\cdot\mathbf{r}} = \frac{1}{\Omega} \mathcal{F}\{ f_{\mathrm{xc}}[\tilde{n}(\mathbf{r})] \}|_{\mathbf{G}_1 - \mathbf{G}_2}. \quad (34)$$

The atom-centered contribution is evaluated on one-dimensional (1D) grids,

$$\Delta K_{\mathbf{G}_1\mathbf{G}_2}^{a,\mathrm{xc-ALDA}} = \frac{1}{\Omega} \int r^2 dr d\hat{\mathbf{r}} e^{-i(\mathbf{G}_1 - \mathbf{G}_2)\cdot\mathbf{r}} [f_{\mathrm{xc}}[n^a] - f_{\mathrm{xc}}[\tilde{n}^a]]. \quad (35)$$

III. NUMERICAL DETAILS

In this section we describe the most important numerical and technical aspects of our implementation: in particular, the Hilbert transform used to obtain χ^0 from the dynamic form factor (spectral function) and the applied parallelization scheme.

A. Symmetry

For each wave vector $\mathbf{q}$, the evaluation of χ^0 involves a summation over occupied and empty states in the entire BZ. By exploiting the crystal symmetries, however, we need only calculate the wave functions and energies in the irreducible BZ (IBZ). This is because the wave function at a general k point can always be obtained from a wave function in the irreducible part of the BZ by application of a symmetry transformation T. In general, we have the relation

$$\psi_{n,T\mathbf{k}}(\mathbf{r}) = \psi_{n,\mathbf{k}}(T^{-1}\mathbf{r}), \quad (36)$$

where $\mathbf{k}$ belongs to the IBZ. The above relation can be directly verified by considering how the right-hand side transforms under lattice translations. In addition to the crystal symmetries, time-reversal symmetry applies to any system in the absence of magnetic fields,

$$\psi_{-\mathbf{k}}(\mathbf{r}) = \psi_{\mathbf{k}}^*(\mathbf{r}). \quad (37)$$

B. Hilbert transform

Rather than constructing χ^0 directly from Eq. (6) we obtain it as a Hilbert transform of the (noninteracting) dynamic form factor, S^0.[32,33] The latter is given by

$$S_{\mathbf{G}\mathbf{G}'}^0(\mathbf{q},\omega) = \frac{2}{\Omega} \sum_{\mathbf{k},nn'} (f_{n\mathbf{k}} - f_{n'\mathbf{k}+\mathbf{q}}) \delta(\omega + \epsilon_{n\mathbf{k}} - \epsilon_{n'\mathbf{k}+\mathbf{q}}) n_{n\mathbf{k},n'\mathbf{k}+\mathbf{q}}(\mathbf{G}) n_{n\mathbf{k},n'\mathbf{k}+\mathbf{q}}^*(\mathbf{G}'). \quad (38)$$

In practice $S^0(\omega)$ is evaluated on a uniform frequency grid extending from 0 to around 40–60 eV with a grid spacing in the range 0.01–0.1 eV, and the δ functions are approximated by triangular functions following Ref. 34. The noninteracting response function is obtained as

$$\chi_{\mathbf{G}\mathbf{G}'}^0(\mathbf{q},\omega) = \int_0^\infty d\omega' S_{\mathbf{G}\mathbf{G}'}^0(\mathbf{q},\omega') \times \left[\frac{1}{\omega - \omega' + i\eta} - \frac{1}{\omega + \omega' + i\eta} \right]. \quad (39)$$

The above Hilbert transform is performed directly on the frequency grid setting the broadening parameter η equal to the grid spacing.

C. LCAO vs grid calculations

It is well known that the use of localized atomic orbitals as basis functions can significantly reduce the computational effort of ground-state electronic structure calculations. For calculations of the density response function the use of localized basis functions is complicated by the fact that such basis sets are typically not closed under multiplication.[35–37] As a consequence, the size of the product basis needed to represent the response function grows as N_μ^2, where N_μ is the number of basis functions used to represent the wave functions (we note that for strictly localized basis functions, the effective size of the "product basis" grows only linearly with the system size because pair densities of nonoverlapping orbitals vanish, however, the prefactor is typically very large). A further challenge is the computation of the Coulomb interaction kernel, $1/|\mathbf{r}-\mathbf{r}'|$, in the product basis leading to six-dimensional multicenter integrals. These intergrals must be performed either by using efficient Poisson solvers or by resorting to analytical techniques. The latter is extensively used in quantum chemistry codes applying Gaussian basis sets.

For these reasons we have chosen to represent the density response function in a plane-wave basis. The plane-wave basis is closed under multiplication and the Coulomb kernel is simply given by Eq. (8). However, we still keep the advantage of using an LCAO as basis in the calculation of the Kohn-Sham wave functions and energies, which enter the construction of χ^0.[27] Apart from reducing the computational effort of the ground-state calculation (which must include many unoccupied bands), the storage requirements for wave functions become much less than for corresponding grid or plane-wave calculations. This is because the LCAO coefficients provide a more compact representation of the wave functions, in particular for open structures containing large vacuum regions, and because significantly fewer unoccupied wave functions result from the LCAO calculation (for a fixed energy cutoff).

Compared to plane waves or real-space grids, LCAO calculations employing standard basis sets usually give a less accurate but often acceptable description of the occupied and low-lying unoccupied wave functions and energies. For higher-lying unoccupied states, blueshifts are expected due to the (unphysical) confinement imposed by the localized basis set, and the continuum is broken into discrete bands. Despite these effects, we have found that the use of LCAO wave functions instead of grid wave functions has rather little effect on the dielectric function—at least in the relevant low-energy regime.

As an example, Fig. 1 shows the absorption spectrum (a) and EELS spectrum (b) of graphene calculated using LDA wave functions and energies from a grid calculation and from an LCAO basis set of varying quality. The unit cell is the primitive cell of graphene containing two carbon atoms and with 20 Å vacuum. The BZ is sampled on a 64×64 Monkhorst-Pack grid. The number of bands included are 60 for the grid and LCAO (qztp) basis and 26 for the LCAO (dzp) basis. In all three cases this corresponds to inclusion of states with energy below 40 eV. The response function is evaluated at the RPA level including local-field effects up to a plane-wave cutoff of 150 eV (465 **G** vectors).

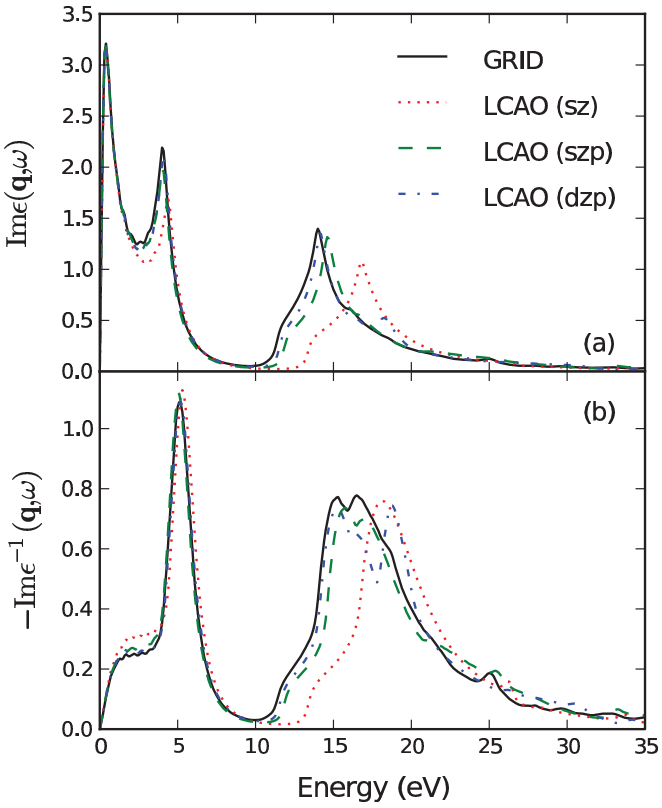

FIG. 1. (Color online) The imaginary part of the dielectric function (a) and energy-loss function (b) of graphene at $q = 0.046$ Å^{-1} along $\bar{\Gamma} - \bar{M}$ direction of its surface Brillouin zone. The LDA wave functions and energies entering χ^0 have been obtained using a 3D uniform grid (black solid line) and a localized atomic orbital (LCAO) containing single ζ (red dotted), single ζ with polarization (green dashed), and double ζ with polarization (purple dashed-dotted), respectively.

For excitation energies below 10 eV, the LCAO results agree remarkably well with the grid calculations. In particular the $\pi \rightarrow \pi^*$ absorption peak at around 4 eV in panel (a) and the π plasmon around 5 eV in panel (b) are well reproduced in LCAO calculations with only the smallest single-ζ (sz) basis set showing small deviations. For energies above 10 eV, we observe slight deviations. However, for the standard szp and dzp basis sets the overall agreement is remarkable for the entire energy range. In particular, the $\sigma \rightarrow \sigma^*$ transition at around 14 eV in panel (a) and the σ plasmon around 17 eV in panel (b) are clearly visible, although in the LCAO (dzp) calculation the latter is split into two peaks.

Figure 2 shows another comparison of a grid- and LCAO-based linear-response calculation for the case of a Mg(0001) surface modeled by a 16-layer slab. The energy-loss function calculated with 3D grids is characterized by two peaks at around 7.5 and 11 eV, which correspond to the surface and bulk plasmons, respectively. Again the LCAO (dzp) calculation reproduces the grid results quite accurately showing only slight discrepancies in the peak positions (around 0.1 eV) and the intensity. Note that dzp basis used in this case includes double-ζ orbitals of $3s$ and $3p$ atomic orbitals as well as one d-type Gaussian polarization function. The inclusion of d-type orbitals in the basis set is crucial for the correct description of

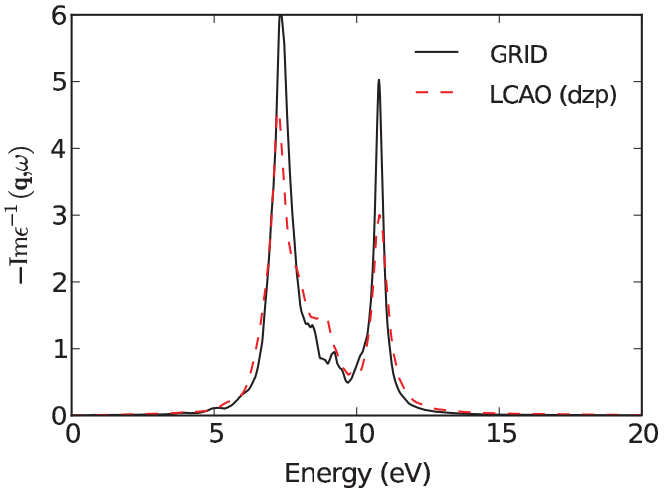

FIG. 2. (Color online) The energy-loss function of Mg(0001) surface at $q = 0.07$ Å^{-1} along $\bar{\Gamma} - \bar{M}$ direction of its SBZ calculated with 3D uniform grid (GRID, black solid line) and localized atomic orbital (LCAO) using dzp (red dashed line) basis. The dzp basis used here includes double-ζ orbitals of $3s$ and $3p$ atomic orbitals as well as one d-type Gaussian polarization function.

both the single-particle band structure and the Mg plasmons. Both the grid and LCAO response function calculations were performed at the ALDA level including empty bands up to 20 eV above the Fermi level. The local fields are included with a 500-eV plane-wave cutoff (corresponding to 317 **G** vectors) in the direction perpendicular to the surface and 10 eV in the surface plane. The small effect of local fields within the surface plane is in agreement with previous results.[38] The frequency grid spacing employed for the Hilbert transform was 0.1 eV.

D. Storage of wave functions

For ground-state calculations performed using grid based wave functions, the entire set of occupied and unoccupied wave functions might be too large to be stored on disk, making the separation of the ground-state and response function calculations impossible. In this case, the response function, or more precisely, the dynamical form factor of Eq. (38), is constructed as the wave functions are calculated.

In the LCAO mode, only the expansion coefficients of the wave functions in terms of the localized basis functions are calculated and stored. Since this representation is significantly more compact than the grid representation, the entire set of wave functions can be calculated and stored at once, and the calculation of the response function can be performed as a postprocessing step.

E. Parallelization

The calculation of the response function involves the three steps: evaluation of the spectral function $S^0_{\mathbf{GG}'}(\mathbf{q},\omega)$ according to Eq. (38), Hilbert transform following Eq. (39), and solving Dyson's equation (5). Figure 3 illustrates the parallelization scheme applied for each of these three steps.

It is natural to parallelize the evaluation of $S^0_{\mathbf{GG}'}(\mathbf{q},\omega')$ over k points (or bands for few k point calculations). On the other hand, the size of the matrix is often too large to be handled on a single CPU. In such cases each CPU only

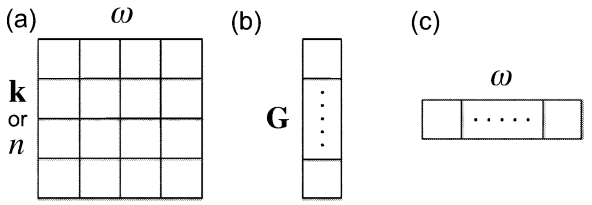

FIG. 3. Schematic illustration of the applied parallelization scheme. Each box represents a single CPU. (a) The calculation of $S^0_{\mathbf{GG}'}(\mathbf{q},\omega)$ is performed in parallel over wave vectors **k** (or bands n, for large cells) and frequencies ω. (b) The Hilbert transform is parallelized over **G**. (c) Finally the Dyson equation is solved by parallelizing over the frequencies.

calculates S^0 on a part of the frequency grid. This leads to the two-dimensional parallelization scheme illustrated in Fig. 3(a). Finally the full $S^0_{\mathbf{GG}'}(\mathbf{q},\omega')$ is obtained by summing over k points, i.e., summing up the columns in Fig. 3(a). Since the Hilbert transform involves a frequency convolution it is convenient to redistribute the data from parallelization over ω to over **G**. Finally, the Dyson equation is done separately for each frequency point and is therefore parallelized over ω, as shown in panel (c).

IV. RESULTS

In this section, the density response function method is applied to study the optical properties and plasmon excitations of solids. They are usually measured by optical and electron energy-loss spectroscopy (EELS), which are related to $\mathrm{Im}\epsilon_M$ and $-\mathrm{Im}[1/\epsilon_M]$, respectively. For extended systems, the two kinds of spectroscopy give quite distinct spectra. The optical-absorption spectrum (ABS) is determined by single-particle excitations while EELS is dominated by collective electronic excitations, plasmons, which are defined as $\epsilon_M \to 0$.

A. Optical properties

Table I shows the calculated RPA static dielectric function in the optical limit for five semiconductors (C, Si, SiC, AlP, GaAs). We use the same lattice constants as in Ref. 30 and a grid spacing of 0.2 Å. A Monkhorst-Pack grid of $12 \times 12 \times 12$ and 60 unoccupied bands are used. We use a Fermi temperature of 0.001 eV in the ground-state LDA calculation and a broadening parameter (η) of 0.0001 eV in χ^0. Note that in this case we calculate the static response function directly from Eq. (6), i.e., we do not use the Hilbert transform. For calculations including local-field effects, a cutoff of 150 eV (169 **G** vectors) is used. The dielectric constants obtained both with and without local fields agree to within 0.1 with previous PAW calculations.[30] The only exception is GaAs, for which our dielectric constant is around 0.4 larger. This deviation could come from differences in the PAW setups for Ga or As. The inclusion of local fields lowers the dielectric constants by 10–15% while the ALDA kernel increases the dielectric constants by around 5%. Both trends are in agreement with earlier reports.[20,40] The fact that the neglect of exchange-correlation effects (at the ALDA level) improves the agreement with experiments can be seen as a consequence of error cancellation between the underscreening provided by RPA and underestimation of the LDA single-particle band gap.

TABLE I. The static macroscopic dielectric constants ϵ calculated using the PAW method with random-phase approximation (RPA) and adiabatic local-density approximation (ALDA) without local field (NLF) and including local field (LF) effect. These values are compared with other PAW calculations (Ref. 30) and experiments (Ref. 39).

Crystal	C	Si	SiC	AlP	GaAs
RPA, NLF	5.98	13.99	7.18	9.04	15.12
RPA, LF	5.58	12.58	6.58	7.83	13.67
ALDA, LF	5.83	13.21	6.89	8.27	14.32
RPA, NLF (Ref. 30)	5.98	14.04	7.29	9.10	14.75
RPA, LF (Ref. 30)	5.55	12.68	6.66	7.88	13.28
ALDA, LF (Ref. 30)	5.82	13.31	6.97	8.33	13.98
Expt. (Ref. 39)	5.70	11.90	6.52	7.54	11.10

Figure 4 shows the dynamical dielectric function for Si. Compared to the calculations for the static dielectric constant, a significantly denser k-point sampling of $80 \times 80 \times 80$ is employed here to resolve the finer details in the spectrum. A total of 36 unoccupied bands are used in the construction of χ^0. Local fields corresponding to a 150-eV plane-wave cutoff are included and η is set to 0.01 eV. The onset of absorption and the position of the two characteristic peaks in the absorption spectrum compare very well with previous RPA calculations[30] as shown by the arrows in the figure. However, it is quite different from the experimental absorption spectrum,[41,42] which exhibits an absorption onset at ~0.5 eV larger than predicted by our calculation, and shows a double peak around 3.8 eV. The effect of local fields and the ALDA kernel is to reduce the intensity of the main absorption peak slightly, in agreement with earlier reports.[40,43,44] The disagreement with the experimental spectrum is due to the underestimation of the band gap by LDA and the fact that ALDA kernel fails to reproduce the electron-hole interaction.

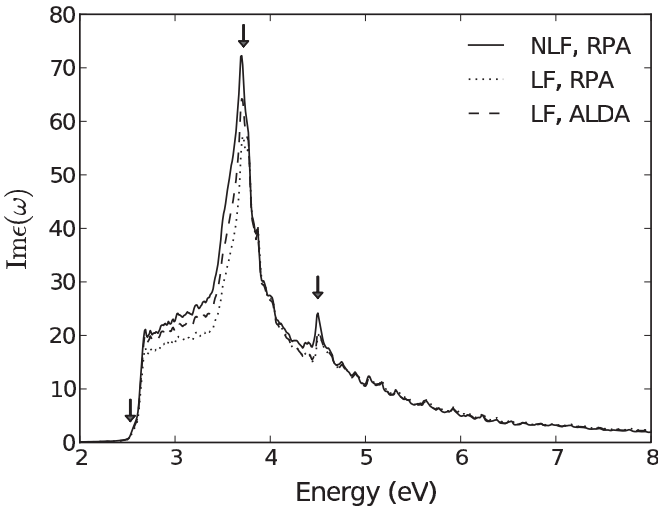

FIG. 4. Imaginary part of the dynamical dielectric function of bulk silicon. The arrows indicate the absorption onset and the position of main and secondary peaks, respectively, as extracted from Ref. 30. Calculations have been performed including local-field effects (dotted and dashed) and exchange-correlation effects at the ALDA level (dashed).

B. Plasmon excitations

In contrast to the optical excitations, like the Si absorption spectrum discussed in the previous section, plasmon excitations are generally well described by RPA and TDLDA. Plasmon excitations appear as strong peaks in the electron energy-loss spectrum (EELS), which is directly related to the imaginary inverse dielectric function,

$$-\mathrm{Im}\epsilon^{-1}(\mathbf{q},\omega) = -\frac{4\pi}{|\mathbf{q}|^2}\mathrm{Im}\chi_{\mathbf{G}=0,\mathbf{G}'=0}(\mathbf{q},\omega). \tag{40}$$

For excitations at surfaces, a surface loss function can be defined as[38]

$$g(\mathbf{q},\omega) = -\frac{2\pi}{|\mathbf{q}|}\iint dz dz' \chi_{\mathbf{G}_\parallel=\mathbf{G}'_\parallel=0}(z,z';\mathbf{q},\omega)e^{|\mathbf{q}|(z+z')}, \tag{41}$$

where $\parallel$ and z correspond to directions parallel and perpendicular to the surface, respectively, and $\chi_{\mathbf{G}_\parallel\mathbf{G}'_\parallel}(z,z';\mathbf{q},\omega)$ is the Fourier transform of $\chi_{\mathbf{G}\mathbf{G}'}(\mathbf{q},\omega)$ in the z direction.

C. Surface plasmons of Mg(0001)

Figure 5 shows the surface loss function of the Mg(0001) surface along the $\bar{\Gamma} - \bar{M}$ direction of the surface BZ calculated within RPA (a) and TDLDA (b). The Mg surface is modeled by a slab of 16 layers as in previous calculations,[38] and a vacuum region of 40 Å. Such a thick slab and vacuum region is necessary to avoid splitting of the surface plasmon peak due to coupling between the surface plasmons at the two sides of the slab. The LDA wave functions are calculated on a uniform grid with a grid spacing of 0.24 Å and a $64 \times 64 \times 1$ Monkhorst-Pack k-point sampling. For the response function calculations we include 200 bands (including 16 occupied bands) and use a broadening parameter of 0.02 eV. We use an anisotropic cutoff energy for the local-field effects. Since the surface plasmon depends sensitively on the density profile at the surface where the density decays exponentially into the vacuum, a cutoff energy of 500 eV is applied in the z direction. In the surface plane, where local-field effects are much less important, we have found it sufficient to use a cutoff energy of 10 eV. Compared to the RPA results in panel (a), the inclusions of the LDA exchange-correlation kernel in panel (b) shifts the peaks down by 0.1–0.2 eV.

The energies of these surface plasmons for both the $\bar{\Gamma} - \bar{M}$ and $\bar{\Gamma} - \bar{K}$ directions are shown in Fig. 5(c). The obtained dispersion relations agree well with previous calculations.[38] The well-known negative dispersion at small $\mathbf{q}$ observed for simple metal surfaces are also well reproduced in this work. Compared to experimental data, the TDLDA energies of the surface plasmons agree within 0.1 eV for small $\mathbf{q}$, while the discrepancy increases to around 0.2 eV for larger $\mathbf{q}$. The fact that the inclusion of exchange-correlation effects (at the ALDA level) brings the plasmon energies in better agreement with experiments is in contrast to the case of the dielectric functions for which the ALDA kernel was found to worsen the agreement with experiments. As already explained, the overestimation of the dielectric function is a direct consequence of the underestimation of the band gap by LDA. For metallic systems this band-gap problem is not present (although interband

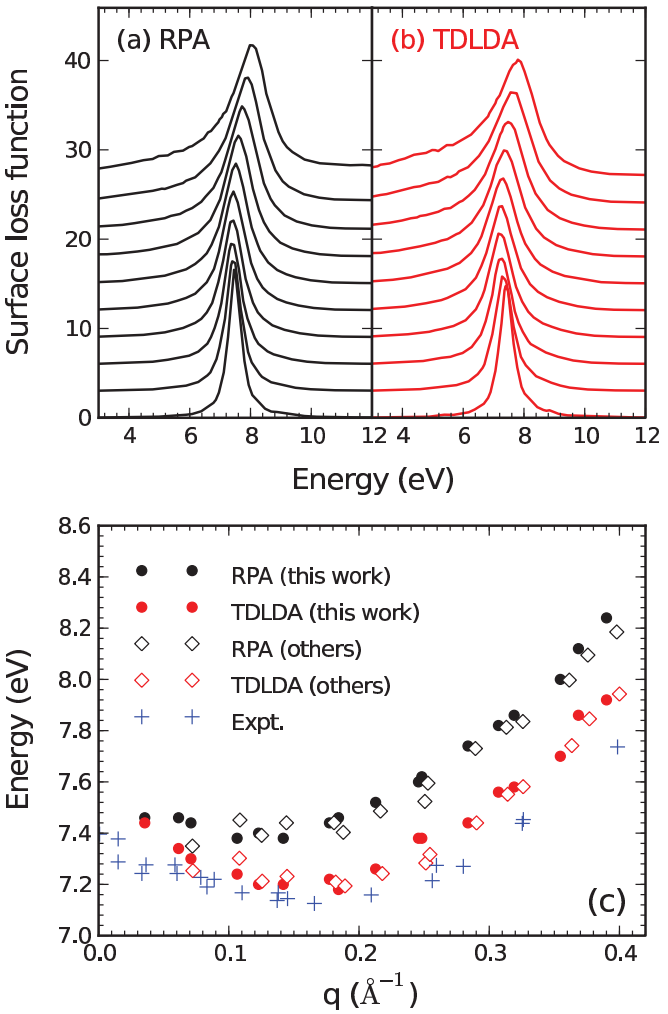

FIG. 5. (Color online) Surface loss function of the Mg(0001) surface along the $\bar{\Gamma} - \bar{M}$ direction of the surface BZ calculated using RPA (a) and TDLDA (b). In both cases $|\mathbf{q}|$ increases from bottom to top. (c) Surface plasmon dispersion for both the $\bar{\Gamma} - \bar{M}$ and $\bar{\Gamma} - \bar{K}$ directions. Results from this work (filled dots) compare well with other calculations (hollow dots, Ref. 38) and experiments, Ref. 45.

transitions may be underestimated) and the inclusion of xc effects correctly lowers the plasmon energies.

D. Plasmons in adsorbed graphene

In this section we investigate the influence of a substrate on the plasmon excitations in graphene. For a more detailed discussion of these results we refer the reader to Ref. 46. As representatives for semiconducting and metallic substrates we consider SiC(0001) and Al(111). Both of these systems are known to bind graphene relatively weakly. Consequently, band-structure effects arising from the hybridization between graphene and metal states are minor for these systems. Instead, the interaction between the graphene and the substrate is expected to be governed by long-range Coulomb interactions. In particular, the collective plasma oscillations in the graphene layer will be mainly affected by the field created by the induced charge oscillations in the substrate.

The atomic structure and band structure of graphene on both substrates are shown in Fig. 6. For graphene/SiC(0001),

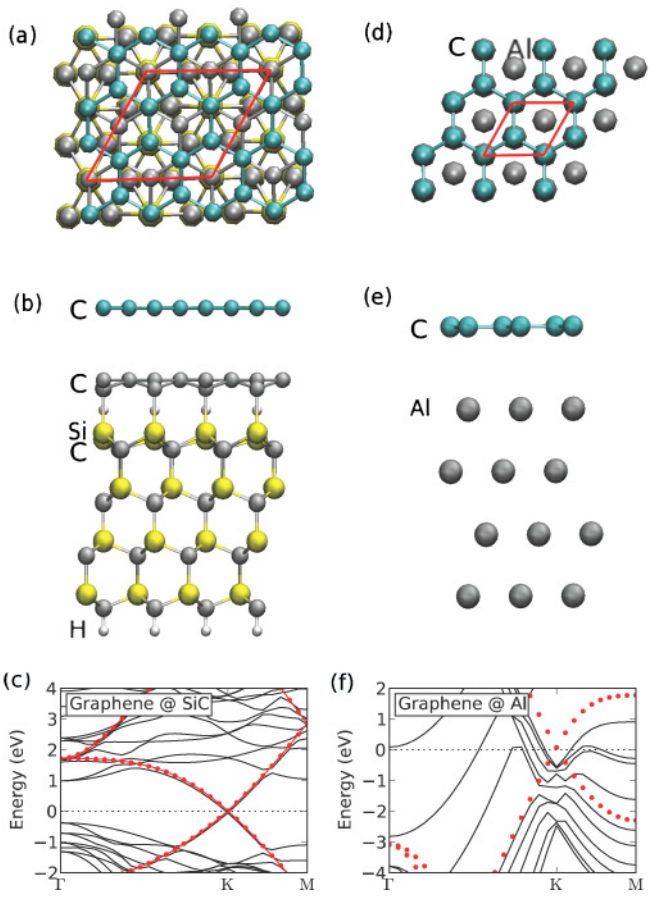

FIG. 6. (Color online) Atomic structure of graphene adsorbed on SiC(0001) (a),(b), and Al(111) (d),(e). The lateral unit cells are indicated by red lines in the top panels. The LDA band structures of the surfaces are shown in the lower panels. Also shown is the band structure of free-standing graphene (red dots). The Fermi level is set to zero.

the unit cell, indicated by red solid lines in panel (a), contains 2×2 graphene and $\sqrt{3} \times \sqrt{3}$ SiC.[47,48] As can be seen in panel (b), two carbon layers are adsorbed on four bilayers of SiC and the dangling bonds at the backside of the slab are saturated by hydrogen. The first carbon layer adsorbs covalently on the SiC surface and is here considered as a part of the substrate. The upper carbon layer binds weakly to the substrate, in agreement with experiments,[49] with an LDA binding energy per C atom of 0.039 eV, and adsorption distance of 3.56 Å. As shown in panel (c), linear conical bands appear within the band gap of the substrate, resembling that of free-standing graphene (red dotted line). The Fermi level is shifted up by 0.05 eV, introducing slight electron doping into graphene. For the graphene/Al(111) structure we use a 1×1 unit cell with four layers of Al as substrate. Again, graphene binds weakly to the Al surface with an LDA interplane distance of 3.36 Å and binding energy per C atom of 0.049 eV, in good agreement with recent van der Waals DFT calculations.[50] As shown in panel (f), the "Dirac cone" of graphene is shifted 0.5 eV below the Fermi level. The loss function is calculated on the basis of wave functions obtained with a double-ζ polarized LCAO basis set. All states with energy below 50 eV above the Fermi level were included in the construction of χ^0. We

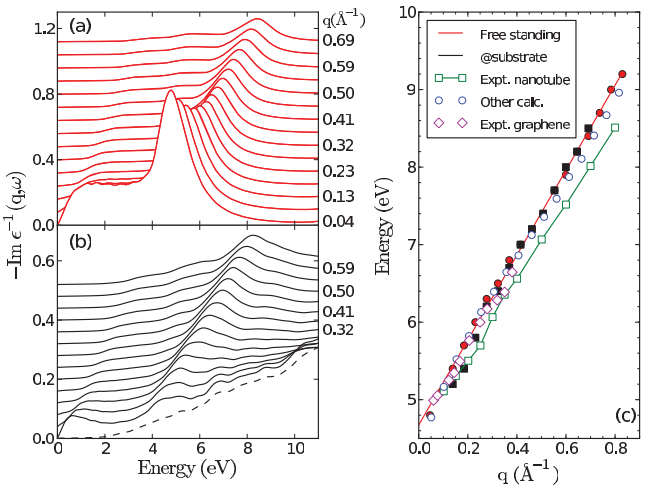

FIG. 7. (Color online) Loss function of free-standing graphene (a) and graphene on SiC substrate (b) as a function of q. The loss functions, from bottom to top (solid lines), correspond to increasing q at an interval of 0.046 Å^{-1}. The dashed line corresponds to the loss function of the substrate at $q = 0.092$ Å^{-1}. (c) Dispersion relations for the π plasmons of free-standing graphene (red filled circles) and graphene on SiC (black filled squares). They are compared with earlier *ab initio* calculation on free-standing graphene (blue hollow circles) and experiments on single-wall carbon nanotubes (green hollow squares) (Ref. 51) as well as experiments on graphene / SiC(0001) (purple hollow diamonds) (Ref. 52). Lines are added to guide the eye.

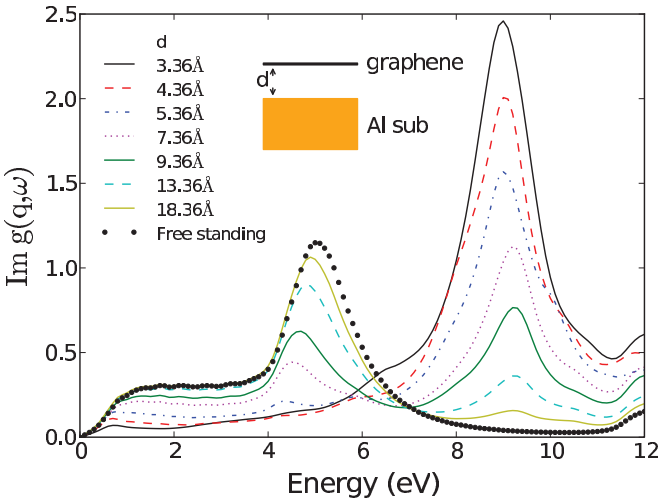

FIG. 8. (Color online) Surface loss functions for graphene on Al(111) as a function of the adsorption distance d for $|\mathbf{q}| = 0.046$ Å^{-1}. The surface loss function of free-standing graphene is shown as black dots. Inset: sketch of graphene on Al substrate.

used a plane-wave cutoff energy of 50 eV (corresponding to 500 **G** vectors) for the local-field effects. We have found that increasing the plane-wave cutoff energy to 500 eV separately in the in-plane and normal directions leads only to minor changes in the EELS spectrum. Further details on the calculations can be found in Ref. 46.

Figure 7 shows the calculated loss function of free-standing graphene (a) and graphene on SiC (b). The free-standing graphene exhibits a collective mode at around 5 eV, which results from the electronic transitions of the $\pi \rightarrow \pi^*$ bands and is referred to as the graphene π plasmon. The dispersion of the π plasmon is shown in Fig. 7(c). In contrast to its three-dimensional counterpart, graphite, which shows a parabolic dispersion of the π plasmons,[13] graphene has a linear plasmon dispersion. The origin of the linear dispersion has been attributed to the role of local-field effects.[51]

Figure 7(b) shows the loss function of graphene adsorbed on the SiC(0001) surface. Compared to the results of the free-standing graphene, the strength of the π plasmons are strongly damped, in particular for small **q** values. As **q** increases, the strength of the π plasmons gradually recovers to that of a free-standing graphene, indicating that the substrate effect becomes weaker for larger **q**. This trend can be explained by the $1/q^2$ dependence of the Coulomb interaction.

As shown in Fig. 7(c), the substrate has little effect on the energies of the π plasmons. In fact the plasmon dispersion for both free-standing and substrate supported graphene agree well with previous calculations[51] as well as experiments on graphene/SiC (Ref. 52) and carbon nanotubes.[51] We have found that the response function, and thus the EELS spectrum, of the combined graphene/substrate system can be obtained accurately from the response functions of isolated graphene and substrate assuming only Coulomb interaction between the two, i.e., neglecting effects related to hybridization and charge transfer.[46] This demonstrates that the strong damping of plasmons results from the nonlocal screening of the graphene plasmon excitation by the substrate electrons.

Figure 8 shows the surface loss function of graphene on Al(111) for various adsorption distances. In contrast to the semiconducting SiC substrate, the π plasmon at 5 eV is completely quenched on the metallic Al substrate at the equilibrium distance $d = 3.36$ Å (full black line). As the graphene is pulled away from the surface, the π plasmon reappears at an energy lower than that of the free-standing graphene. This downshift is due to the coupling to the surface plasmons of the aluminum substrate at 9.0 eV. The graphene π plasmon is only fully recovered at a distance of around 20 Å, illustrating the long-range nature of the interaction.

V. CONCLUSIONS

We have implemented the linear density response function in the adiabatic local-density approximation (ALDA) within the real-space projector augmented wave method GPAW, and used it to calculate optical and dielectric properties of a range of solids, surfaces, and interfaces. The Kohn-Sham wave functions, from which the response function is built, can be obtained either on a real-space grid or in terms of localized atomic-orbital basis functions. The latter option reduces the computational requirements for calculating and storing the often very large number of wave functions required for the construction of the response function without sacrificing accuracy. The dielectric constants of a number of bulk semiconductors as well as the optical-absorption spectrum of silicon at the ALDA level was shown to be in good agreement with previous calculations. For the surface plasmons of the Mg(0001) surface we find, in agreement with previous studies, that the ALDA kernel lowers the plasmon energies by around 0.3 eV realtive

to the RPA values and thereby reduces the deviation from experiments from around 4% to 1–2%. Very good agreement with experiments was also found for the plasmon energies of graphene, which were shown to exhibit a linear dispersion with a value of 4.9 eV in the long-wavelength limit. The deposition of graphene on a SiC substrate is shown to have little effect on the plasmon energies but leads to significant damping of the plasmon resonances. In contrast deposition on an Al surface completely quenches the graphene plasmons due to strong nonlocal electronic screening effects.

ACKNOWLEDGMENTS

The Center for Atomic-scale Materials Design is sponsored by the Lundbeck Foundation. The Catalysis for Sustainable Energy initiative is funded by the Danish Ministry of Science, Technology and Innovation. The computational studies were supported as part of the Center on Nanostructuring for Efficient Energy Conversion, an Energy Frontier Research Center funded by the US Department of Energy, Office of Science, Office of Basic Energy Sciences under Award No. DE-SC0001060.

*thygesen@fysik.dtu.dk

[1] E. Runge and E. K. U. Gross, Phys. Rev. Lett. **52**, 997 (1984).
[2] S. Botti, A. Schindlmayr, R. D. Sole, and L. Reining, Rep. Prog. Phys. **70**, 357 (2007).
[3] M. E. Casida, C. Jamorski, K. C. Casida, and D. R. Salahub, J. Chem. Phys. **108**, 4439 (1998).
[4] S. L. Adler, Phys. Rev. **126**, 413 (1962).
[5] N. Wiser, Phys. Rev. **129**, 62 (1963).
[6] M. S. Hybertsen and S. G. Louie, Phys. Rev. B **35**, 5585 (1987).
[7] J. M. Pitarke, V. M. Silkin, E. V. Chulkov, and P. M. Echenique, Rep. Prog. Phys. **70**, 1 (2007).
[8] M. Rocca, Surf. Sci. Rep. **22**, 1 (1995).
[9] A. A. Quong and A. G. Eguiluz, Phys. Rev. Lett. **70**, 3955 (1993).
[10] A. Marini, R. Del Sole, and G. Onida, Phys. Rev. B **66**, 115101 (2002).
[11] K.-D. Tsuei, E. Plummer, A. Liebsch, E. Pehlke, K. Kempa, and P. Bakshi, Surf. Sci. **247**, 302 (1991).
[12] B. Diaconescu *et al*., Nature (London) **448**, 57 (2007).
[13] A. G. Marinopoulos, L. Reining, V. Olevano, and A. Rubio, Phys. Rev. Lett. **89**, 076402 (2002).
[14] R. Hambach, C. Giorgetti, F. Sottile, L. Reining,N. Hiraoka, Y. Q. Cai, A. G. Marinopoulos, and F. Bechstedt, Phys. Rev. Lett. **101**, 266406 (2008).
[15] S. Waidmann, M. Knupfer, B. Arnold, J. Fink, A. Fleszar, and W. Hanke, Phys. Rev. B **61**, 10149 (2000).
[16] V. Olevano and L. Reining, Phys. Rev. Lett. **86**, 5962 (2001).
[17] W. Ku, W. E. Pickett, R. T. Scalettar, and A. G. Eguiluz, Phys. Rev. Lett. **88**, 057001 (2002).
[18] J. Harl and G. Kresse, Phys. Rev. Lett. **103**, 056401 (2009).
[19] M. Städele, J. A. Majewski, P. Vogl, and A. Görling, Phys. Rev. Lett. **79**, 2089 (1997).
[20] M. S. Hybertsen and S. G. Louie, Phys. Rev. B **34**, 5390 (1986).
[21] G. Onida, L. Reining, and A. Rubio, Rev. Mod. Phys. **74**, 601 (2002).
[22] E. E. Salpeter and H. A. Bethe, Phys. Rev. **84**, 1232 (1951).
[23] J. J. Mortensen, L. B. Hansen, and K. W. Jacobsen, Phys. Rev. B **71**, 035109 (2005).
[24] J. Enkovaara *et al*., J. Phys.: Condens. Matter **22**, 253202 (2010).
[25] P. E. Blöchl, Phys. Rev. B **50**, 17953 (1994).
[26] P. E. Blöchl, C. J. Först, and J. Schimpl, Bull. Mater. Sci. **26**, 33 (2003).
[27] A. H. Larsen, M. Vanin, J. J. Mortensen, K. S. Thygesen, and K. W. Jacobsen, Phys. Rev. B **80**, 195112 (2009).
[28] B. Adolph, J. Furthmüller, and F. Bechstedt, Phys. Rev. B **63**, 125108 (2001).
[29] H. Ibach and D. L. Mills, *Electron Energy Loss Spectroscopy and Surface Vibrations* (Academic, New York, 1982).
[30] M. Gajdoš, K. Hummer, G. Kresse, J. Furthmüller, and F. Bechstedt, Phys. Rev. B **73**, 045112 (2006).
[31] G. Grosso and G. P. Parravicini, *Solid State Physics* (Academic, San Diego, 2000).
[32] A. Marini, C. Hogan, M. Grüning, and D. Varsano, Comput. Phys. Commun. **180**, 1392 (2009).
[33] Z. Yuan and S. Gao, Comput. Phys. Commun. **180**, 466 (2009).
[34] M. Shishkin and G. Kresse, Phys. Rev. B **74**, 035101 (2006).
[35] W. Hanke and L. J. Sham, Phys. Rev. B **12**, 4501 (1975).
[36] F. Aryasetiawan and O. Gunnarsson, Phys. Rev. B **49**, 16214 (1994).
[37] S. Brodersen, D. Lukas, and W. Schattke, Phys. Rev. B **66**, 085111 (2002).
[38] V. M. Silkin, E. V. Chulkov, and P. M. Echenique, Phys. Rev. Lett. **93**, 176801 (2004).
[39] P. Y. Yu and M. Cardona, *Fundamentals of Semiconductors* (Springer-Verlag, Berlin, 2001).
[40] V. I. Gavrilenko and F. Bechstedt, Phys. Rev. B **55**, 4343 (1997).
[41] D. E. Aspnes and A. A. Studna, Phys. Rev. B **27**, 985 (1983).
[42] S. Albrecht, L. Reining, R. Del Sole, and G. Onida, Phys. Rev. Lett. **80**, 4510 (1998).
[43] V. I. Gavrilenko and F. Bechstedt, Phys. Rev. B **54**, 13416 (1996).
[44] B. Arnaud and M. Alouani, Phys. Rev. B **63**, 085208 (2001).
[45] P. T. Sprunger, G. M. Watson, and E. W. Plummer, Surf. Sci. **269**, 551 (1992).
[46] J. Yan, K. S. Thygesen, and K. W. Jacobsen, Phys. Rev. Lett. **106**, 146803 (2011).
[47] F. Varchon *et al*., Phys. Rev. Lett. **99**, 126805 (2007).
[48] A. Mattausch and O. Pankratov, Phys. Rev. Lett. **99**, 076802 (2007).
[49] K. V. Emtsev, F. Speck, T. Seyller, L. Ley, and J. D. Riley, Phys. Rev. B **77**, 155303 (2008).
[50] M. Vanin, J. J. Mortensen, A. K. Kelkkanen, J. M. Garcia-Lastra, K. S. Thygesen, and K. W. Jacobsen, Phys. Rev. B **81**, 081408 (2010).
[51] C. Kramberger *et al*., Phys. Rev. Lett. **100**, 196803 (2008).
[52] J. Lu, K. P. Loh, H. Huang, W. Chen, and A. T. S. Wee, Phys. Rev. B **80**, 113410 (2009).